A piezo-shunted kirigami auxetic lattice for adaptive elastic wave filtering

Morvan Ouisse[1], Manuel Collet[2], Fabrizio Scarpa[3]

[1] FEMTO-ST - Department of Applied Mechanics - UMR CNRS 6174 - ENSMM - Univ. Bourgogne Franche-Comté (UBFC) - Besançon - France
[2] LTDS - UMR CNRS 5513 - ECL - Lyon University - Écully- France
[3] ACCIS - Queens School of Engineering, Department of Aerospace Engineering - University of Bristol - Bristol - United Kingdom

E-mail: morvan.ouisse@femto-st.fr manuel.collet@ec-lyon.fr, and F.Scarpa@bristol.ac.uk

Abstract. Tailoring the dynamical behavior of wave-guide structures can provide an efficient and physically elegant approach for optimizing mechanical components with regards to vibroacoustic propagation. Architectured materials as pyramidal core kirigami cells combined with smart systems may represent a promising way to improve the vibroacoustic quality of structural components. This paper describes the design and modelling of a pyramidal core with auxetic (negative Poisson's ratio) characteristics and distributed shunted piezoelectric patches that allow for wave propagation control. The core is produced using a kirigami technique, inspired by the cutting/folding processes of the ancient Japanese art. The kirigami structure has a pyramidal unit cell shape that creates an in-plane negative Poisson's ratio macroscopic behavior. This structure exhibits in-plane elastic properties (Young's and shear modulus) which are higher than the out-of-plane ones, and hence this lattice has very specific properties in terms of wave propagation that are investigated in this work. The short-circuited configuration is first analysed, before using negative capacitance and resistance as a shunt which provides impressive band gaps in the low frequency range. All configurations are investigated by using a full analysis of the Brillouin zone, rendering possible the deep understanding of the dynamical properties of the smart lattice. The results are presented in terms of dispersion and directivity diagrams, and the smart lattice shows quite interesting properties for the adaptive filtering of elastic waves at low frequencies bandwidths.

PACS numbers: 46.40.-f, 77.84.Lf, 62.30.+d

Keywords: periodic structures, elastic wave propagation, band gaps, piezoelectric shunt, kirigami, auxetic structures

Submitted to: *Smart Mater. Struct.*

1. Introduction

Embedding smart materials in structures appears to be a very efficient way to provide new functionalities to users. In this work we focus on the dynamical behavior of two-dimensional waveguides which are designed such that they can bring new properties in terms of elastic wave propagation, with a particular focus on the adaptivity of the system. Structures with smart mechanical behavior are most of the time designed for static and low frequency performances (see [1, 2, 3] among many others). Recently, research activities have been developed to design new multi-functional structures that integrate electro-mechanical systems able to control their vibroacoustic behavior over a wide frequency band [4, 5]. However, there is still a lack of studies in open literature related to the medium frequency (MF) optimization of the structural vibration. This paper is related in particular to this topic, with a focus on the ability of controlling elastic waves in auxetic lattices whose behavior is tuned with piezoelectric patches shunted with electric circuits. The work shown in this paper offers a contribution towards the solving of the challenges of the design and implementation of new classes of integrated smart metacomposites capable of improving the engineering performance in terms of mechanical and vibroacoustic behavior, as compared to strictly passive structures. We are interested here on the class of metacomposites that combine two different aspects of vibration control, namely the concept of periodic structures and the ability to change the mechanical behavior of structures using smart materials.

Recent research works about periodic structures are often presented as inspired by developments related to metamaterials, in particular within the context of light propagation. Many research efforts have been undertaken to investigate ways to design and construct photonic crystals exhibiting photonic band gaps that prevent light from propagating in certain directions at specific frequencies, or able to propagate light in anomalous and useful ways (i.e. negative refraction and artificial magnetism). These concepts can be extended to acoustic or elastic waves, defining the so-called phononic crystals which consists in periodic arrangement of the media in which the waves propagates in order to build interferences and/or diffraction effects that radicaly change the dispersion properties [6]. The position of the Bragg band gap in the frequency domain is directly related to the spatial period of the crystal. This is interesting from the designer's point of view, but quite limited for practical applications in the audible frequency range in which the wavelengths of interest may be of dozens of centimetres or meters. An efficient way to eliminate this constraint consists in using locally resonant unit cells. In such approach a new frequency gap is opened around the resonance frequency, which may be tuned by changing the mass or stiffness of the resonator. [7] had demonstrated that a resonant sonic crystal including rubber-coated lead balls exhibits a low-frequency sonic band gap, and the resonance can provide a maximum impedance mismatch to shield against airborne sound. The same effect can be obtained using Helmoltz resonators as showed by Fang et al. [8, 9] or Hu [10]. Similar techniques can be applied to control propagation of elastic waves in structures [11]. One of the ways

to add a resonant system to the structure of interest without modifying substantially an original design consists in using piezoelectric patches, which are shunted with RL circuits [12]. The work of Hagood and Von Flotow [13] should be mentioned as a precursor in this strategy, with practical design rules that still remain used today. The tunable characteristics of shunted piezo-patches allow the equivalent mechanical impedance of the structure to be tuned so that stop bands are generated over desired frequency ranges. The presence of a resistance in the shunt circuit generates a damped resonance of the electrical network. The resistance also allows the energy dissipation mechanism of shunted piezos to be exploited, which dampens the amplitude of vibrations also outside the stop bands. The original periodic shunting concept was numerically demonstrated on rods and fluid-loaded axisymmetric shells in [4], before being extended to plates [14, 15, 16], where the Bloch theorem was used to predict the dispersion properties of the resulting periodic structure. This kind of approach inspired many recent contributions, and the research work for developing tools that can help engineers to design such systems is high [17, 18]. However, the main limitation of this approach is the narrow-band effectiveness of the resonant circuits. An alternative originally proposed by Forward [19] consists in using negative capacitance shunts. By tuning this capacitance in accordance with the effective capacitance of the embedded patch, the total impedance of the shunt circuit reduces to that of the remaining circuit, which opens the way to any arbitrary frequency-dependent effective impedance, that finally provides the desired behavior to the structure. Using this kind of approach for effective determination of the proper electrical impedance requires the use of optimization algorithms [20, 21], hence allowing the frequency bands of interest to be extended in very large ways. Although the negative capacitance shunting strategy has been experimentally validated, it must be used with caution since it requires active elements that can destabilize the structure if improperly tuned [22, 23]. Efficiency band and stability can be improved by using specific parameters and circuit architecture [24]. This strategy may be followed to design new reconfigurable systems that can handle several functions with a single shunt circuit, allowing for example an effective change from wideband absorption to wideband reflection of elastic [25, 26, 27] or acoustic waves [28, 29]. Electrical shunts may also reproduce physical phenomenon with analog components [30, 31]. These works all contribute to the development of what has been called programmable matter by Toffoli [32] to refer to an ensemble of computing elements arranged in space, now extended to smart materials based on distributed piezoelectric actuators able to modify the inherent vibroacoustic properties of a given structure.

Innovative manufacturing techniques have been recently developed for the production of composite structures with complex shapes and functions [33, 34], and the kirigami process is one of them. kirigami is the ancient Japanese art of folding and cutting paper and has been applied to produce complex 3D cellular structures using modular moulding techniques [35, 36, 37], foldable structures [38], robotic devices [39] and nanoscale artificial materials [40]. The interest reader may find a review of origami and kirigami engineering applications in [41]. Negative Poisson's ratio (or auxetic)

solids have been extensively studied during the past three decades [42, 43]. The term auxetics covers a wide range of materials and structures exhibiting a negative Poisson's ratio. In cellular configurations, a negative Poisson's ratio can be achieved in re-entrant centre-symmetric (butterfly) honeycombs [44, 45], rotating rectangles and triangles [46], as well as arrow-head [47] and star-shaped configurations [48]. The centre-symmetric auxetic configuration has also been considered as a basis for gradient cellular structures [49, 50]. In a more general way, strategies allowing tailoring of mechanical properties [51] have reported for obtaining a Poisson's ratio up to -1 in 2D [52] or 3D [53]. All these configurations have been investigated in terms of manufacturing possibilities and mechanical performances, mainly in the static domain. However, new research activities in the areas of vibroacoustics of auxetic structures have been performed in recent years. The negative Poisson's ratio, which provides an unusual large volume deformation during loading induces tunable wave propagation directivities not commonly observed in classical systems. Recently, some kirigami auxetic cellular structures have also been deeply investigated in terms of wave propagation [54] and the concept has been pushed toward its limits with a null Poisson's ratio that induces negative stiffness regime under nonlinear deformation and high energy dissipation under cyclic loading [55]. Readers may refer to the recent monograph that summarizes major landmark works in auxetics research and development [56].

Among the properties of interest for wave propagation in smart periodic structures, the directionality has been little investigated [54, 57]. However, the adaptive character of the electrical shunts may be a very efficient way to force the waves to follow a path of interest, for several purposes like isolation or energy harvesting. In this paper, we numerically investigate a strategy for controlling directionality properties of a kirigami auxetic lattice with the pyramidal topology described in [54]. Pyramidal lattices have been developed in recent years as lightweight cores for energy absorption [58, 59, 60] and unusual stretchable-bendable composites [61]. Concerning the kirigami pyramidal lattice of reference [54], the unusual deformation properties and its wave propagation characteristics are also due to the fact that the system is only partially auxetic [62], i.e., it exhibits auxetic behaviour only in the xy and yx planes. It is also worth noticing that a theoretical negative Poisson's ratio effect may be even induced in these structures if a geometrical perturbation of the lattice architecture is applied [63]. Moreover, since 1987 it is known that it is not necessary to arrange auxetic structures by hand such structures, even in the isotropic case, can be obtained by a spontaneous self-organization of properly selected objects. Such objects can be hard, as in [64] or soft [65]. Obviously, depending on the shape of the objects forming them, the obtained structures can be auxetic or not, and can have various symmetries as illustrated, e.g. in [66].

The control is achieved through the use of shunted piezoelectric patches glued onto a periodical distribution of auxetic composite cells. This combination of both property induced by auxeticity and negative shunt circuit is analyzed in terms of wave propagation properties. This controlling capability is obtained by correctly tuning the parameters of the external circuit by which almost arbitrary effective structural

impedance may be obtained. The particular bandwidth considered in this work (0 to 2.5 kHz) is typical of low frequency ranges excitations in most large scale airframe and transport structures. As it will be clear from the numerical results shown in the following paragraphs, the rich wave dispersion behaviour of this lattice in that particular bandwidth makes it particularly suitable as an active material vibration control platform for potential vibroacoustic applications at low frequencies. The paper is organized as follows: section 2 presents the structure of interest, section 3 recalls the methodology which has been applied here, section 4 provides the properties of the smart lattice when all piezoelectric patches are short-circuited, section 5 is dedicated to the analysis of the impact of a negative capacitance as shunt, section 6 considers the addition of a resistance in the shunt circuit, and conclusions are derived about the properties in terms of wave propagation of the smart kirigami auxetic lattice.

2. Description of the piezo-shunted kirigami auxetic lattice

In this section, the piezo-shunted kirigami auxetic lattice is described. Following the concept introduced in [54], the lattice is composed by a periodic distribution of kirigami -produced unit cells from kevlar/epoxy prepregs (Kevlar 49/914). Each cell includes shunted piezoelectric patches located on the base of the structure, as shown in figure 1.

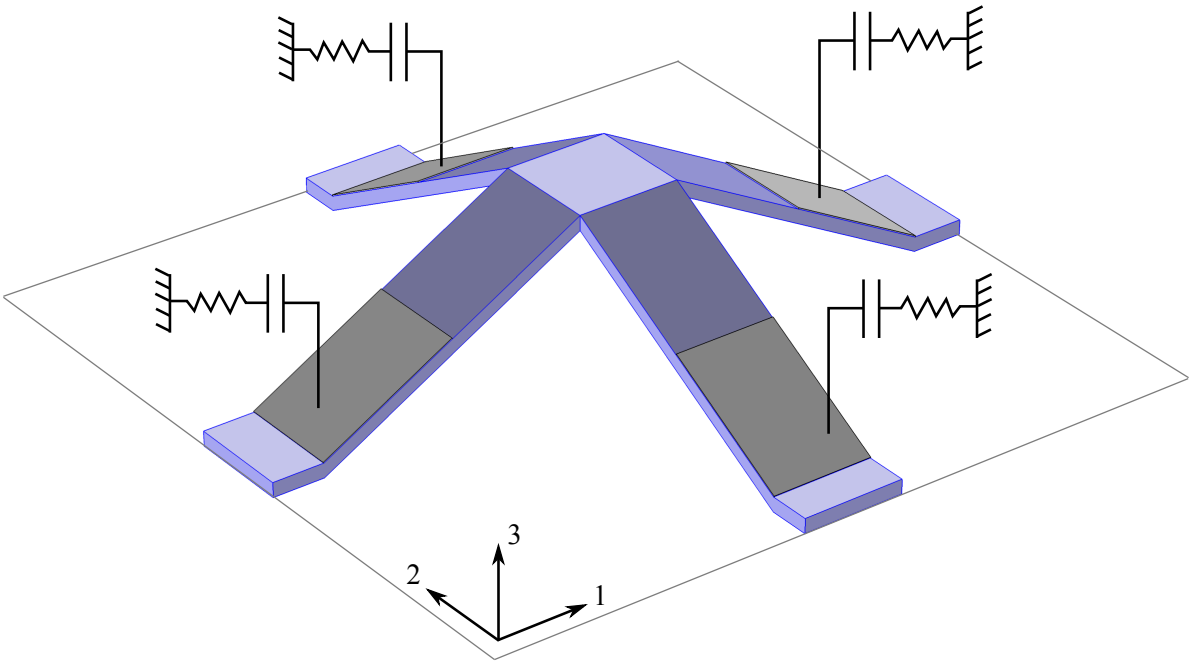

Figure 1. The piezocomposite periodic auxetic cell

The mechanical properties of the host structure material are a Young's modulus of 30 GPa, Poisson's ratio of 0.4, loss factor of 10^{-3} and density equal to 1600 kg.m^{-3}. The unit cell is a 120×120 mm^2 square, the legs are 17 mm width, 2.5 mm thick. The

geometric configuration of the lattice was similar to the one shown in reference [54]. The in-plane Poisson's ratios $\nu_{xy} = \nu_{yx}$ was -0.88, corresponding to a set of dimensionless parameters $\theta = 25^o$ and $\delta = 5.0$. The piezoelectric patches are located at the bottom of the legs, they are 17 mm width, 25 mm long and 0.2 mm thick. The angle formed by the legs is such that the height of the central square is 25 mm. The piezoelectric ceramic is Lead Zirconate Titanate (PZT-4) [67].

In the various configurations that will be investigated in this paper, the four patches may have an off/on shunt a pure negative capacitance (called Cneg) or a negative capacitance with resistance (called RCneg) circuit. The negative capacitance chosen is related to the cell instability point: an increase of the absolute value of the shunt capacitance results in a decrease of the effective cell stiffness until instability occurs. Figure 2 illustrates the change in the value of the first complex eigenfrequencies of the clamped-clamped cell when negative capacitance ratio α changes. This ratio is defined as $C_{neg} = -\alpha C_o$ where $C_o = 12.68\ nF$ is the effective capacitance of the glued piezoelectric patch. The figure shows that one of the eigenfrequencies becomes imaginary for $\alpha = 1.61$. This corresponds to the optimal point to tune the imaginary part of the electrical impedance [20, 25, 26, 27, 24].

The shunt circuit may also include an electrical resistance to impact the frequency efficiency of the system [24, 25]. In the following computations, both $R = 0$ (pure C_{neg} circuit) and $R = 500\Omega$ are used. Investigations presented in the paper will include results on the impact on the directivity of the lattice when dissipative elements are included in the shunt circuit [25, 26]. In order to distinguish the various configurations, the 4 branches of the unit cell are identified through cardinal directions (W, N, E, S). The E direction is aligned with direction 1 in figure 1, and corresponds to the reference axis for the angle φ that will be defined later. The N direction is aligned with direction 2 in figure 1. The lattice is obtained by repeating the unit cell in EW and NS directions, as illustrated in figure 3.

3. Methods and indicators for the dispersion analyses of the smart lattice

The dispersion diagrams are evaluated using the approach described in [21]. The computational method consists in reformulating the Floquet-Bloch theorem for computing waves dispersion for periodically smart distributed mechanical systems incorporating electronic components, damping effects or any frequency-dependent characteristics. The finite element approach used in this work is based on a fully 3D formulation of the periodic piezo elastodynamic problem introducing the wave number as the unknown eigenvalue of the the Floquet-Bloch shift cell operator [68]. The mesh size has been chosen to guarantee the convergence of the method in accordance to reference [68]. Simulations are performed on the first Brillouin zone of the lattice [69]. The shape of this zone changes, depending on the symmetry of the problem, which may be broken when non identical shunt circuits are chosen in the various branches of the cell. In any case, the whole Brillouin zone is investigated to understand properly the properties of

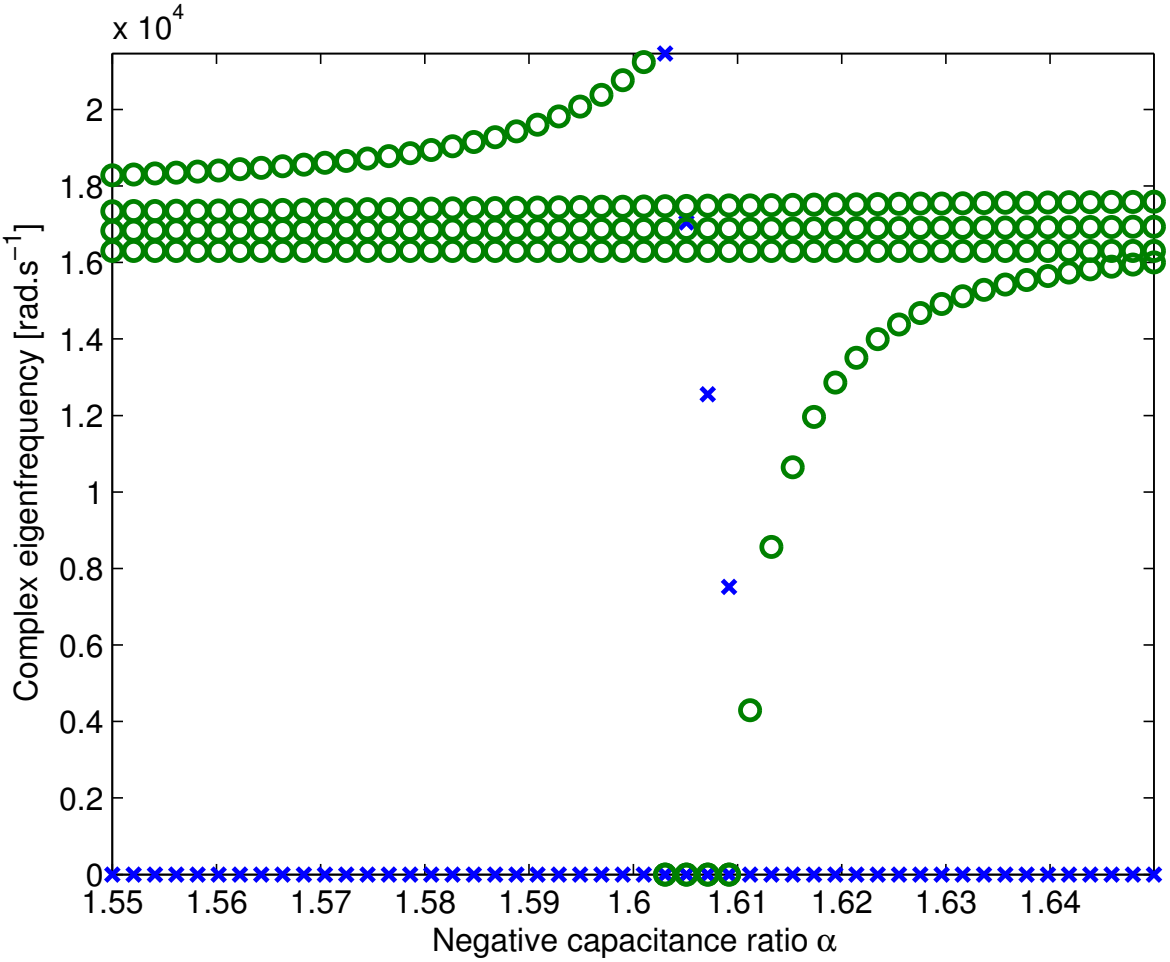

Figure 2. Complex eigenfrequencies of clamped-clamped cell [rad.s^{-1}] vs. negative capacitance ratio α: ○ real part, × imaginary part

the system in terms of wave propagation. Following this objective, the frequency ω is fixed, together with the wave angle φ in the reciprocal space, and the wave number k is computed through a generalized eigenvalue problem. The problem being damped from the structural loss factor and by the piezoshunt coupling, k is complex. Its real part corresponds to propagative component, while its imaginary part is related to spatial attenuation. The wave number vector $\boldsymbol{k}$ has $k\cos\varphi$ and $k\sin\varphi$ components in the plane. Finally, ω is varied on the frequency range of interest, and θ is varied to cover the first Brillouin zone and the eigenvalue problem is solved for each configuration.

For each solution, the group velocity [70] is computed by

$$\boldsymbol{C}_{g_n}(\omega,\varphi) = \nabla_{\boldsymbol{k}}\omega = \frac{\langle\langle \boldsymbol{S}\rangle\rangle}{\langle\langle e_{tot}\rangle\rangle} = \frac{\langle \boldsymbol{I}\rangle}{\langle E_{tot}\rangle} \tag{1}$$

where $\langle\langle:\rangle\rangle$ is the spatial and time average respectively on one cell and one period of time, $\boldsymbol{S}$ is the density of energy flow, $\boldsymbol{I}$ the mean intensity and e_{tot}, E_{tot} the total energy and its time average on a period (see [70] for details).

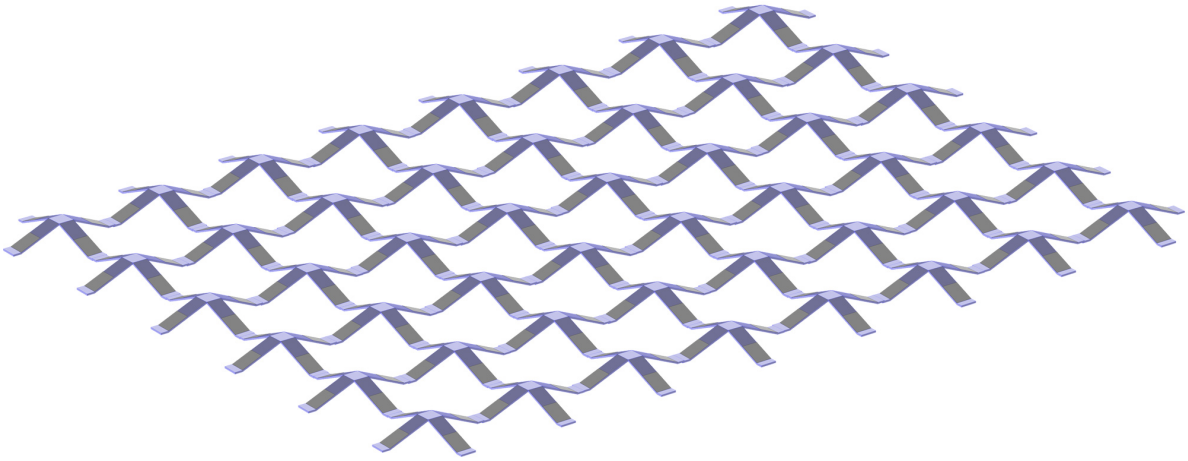

Figure 3. The piezocomposite lattice

Due to the geometry and physical complexity of the lattice, the eigenvalue solver may return a very large number of solutions. Adequate filtering is necessary in order to determine the outputs of interest for the understanding of the physical phenomenon arising in this metacomposite. Hence two criteria are used for filtering the waves. The first one restricts the analysis only to wave numbers with real parts inside the first Brillouin zone, ie

$$\mathrm{Re}(k) < \tau_{BZ} k_{BZ}(\varphi) \tag{2}$$

where $k_{BZ}(\varphi)$ is the length of the line investigated in the Brillouin zone at angle φ and τ is a threshold. Due to the shape of the Brillouin zone (square or triangle depending on the possible symmetry in the shunts),

$$k_{BZ}(\varphi) = \frac{\pi}{L\cos\varphi} \quad \text{for} \quad \varphi \in \left[0\,;\,\frac{\pi}{4}\right] \tag{3}$$

or

$$k_{BZ}(\varphi) = \frac{\pi}{L\cos(\pi/2-\varphi)} \quad \text{for} \quad \varphi \in \left[\frac{\pi}{4}\,;\,\frac{\pi}{2}\right] \tag{4}$$

where L is the length of the square cell (120 mm for the considered case). τ should theoretically have a value of 1, but numerical issues may provide wave number with real parts slightly lower than $k_{BZ}(\varphi)$. This is the reason why in the numerical presented hereafter, a value of $\tau_{BZ} = 0.99$ has been used. The second criterion is related to the evanescent nature of the waves of interest. In the work described in this paper, both damping in the physical model of the structure and complex electrical impedance used to shunt the piezoelectric patch provide complex wave numbers as solutions of the eigenvalue problem [68]. The waves of interest for describing the dynamical behavior of the smart kirigami lattice being those that can propagate over several wavelengths, the highly evanescent waves may be removed from the dispersion diagrams. They are computed and correspond to important signature of the structure, in particular for the determination of the forced response of the system, but do not correspond to propagative

effects of interest in this paper. The complexity of the wavenumber may be quantified by the ratio of imaginary part to its real part, hence only waves that verify

$$\frac{|\text{Imag}(k_n)|}{|\text{Real}(k_n)|} \leq \tau_e \tag{5}$$

are considered in the analysis. Real$(\cdot)$ stands for real part and Imag$(\cdot)$ for imaginary part. In the results presented hereafter, a value of $\tau_e = 0.8$ has been used. It should be emphasized that this value is quite high since it corresponds to 96% of reduction in amplitude after a single wavelength. A lower value of τ_e may be used to be more selective on the waves of interest. Finally, high-order evanescent waves appearing in the spectrum as quadruplets of eigenvalues $(k_n,\ \bar{k}_n,\ -k_n,\ -\bar{k}_n)$ are also removed from the analysis [70].

4. Short-circuited reference configuration

4.1. Dispersion along $\Gamma - X$ direction of the short-circuited reference configuration

The dispersion curves of the system along the Brillouin zone $\Gamma - X$ direction (i.e for $\varphi = 0$) are shown in figure 4 for a closed circuit (ie, the piezo electrodes are in short circuit). The figure shows the real part of the non dimensional wavenumbers defined as $\dfrac{k_n(\omega, \varphi)}{k_{BZ}(\varphi)}$ when no filtering is applied. As expected, numerous solutions are found, highlightning both the rich wave dispersion behaviour but also the complexity of the involved analysis.

After applying the three filters with $\tau_{BZ} = 0.99$ and $\tau_e = 0.8$, the dispersion diagram shown in figure 5 is obtained. It should be recalled that the calculations are performed by making ω varying in the frequency range of interest, which explains the fact that the dispersion curves do not reach the 0 and 1 values of the reduced wave number. A refined frequency step in the analysis would bring the dispersion curves to the borders of the domain. The links between the dots is done by tracking the shapes of the eigenvectors using a correlation criteria [68]. The results show the complexity of the vibroacoustic behavior of the system with three band gaps in the frequency range of interest, namely 0 to 2500 Hz. Between these band gaps, several waves are able to transport energy along the lattice. All dispersion diagrams presented hereafter use the same filters.

The modes occurring with the highest wavenumber at low frequencies correspond to an out-of-plane movement with propagation along the $\Gamma - X$ axis, with the transverse legs moving creating a macroscopic flexural effect that can be compared to the first antisymmetric Lamb-wave mode (often called A_0) associated with the largest wavenumber in the low frequency band. An example is shown in figure 6, corresponding to the red box in figure 5. It should be emphasized that all shapes presented in the figures of this paper are associated to the propagation direction 1 (see figure 1 for the system of reference), ie EW or $\varphi = 0$. Moreover, the terminology used for the discrimination refers to this direction. In order to help readers to understand the behavior of the structure, in

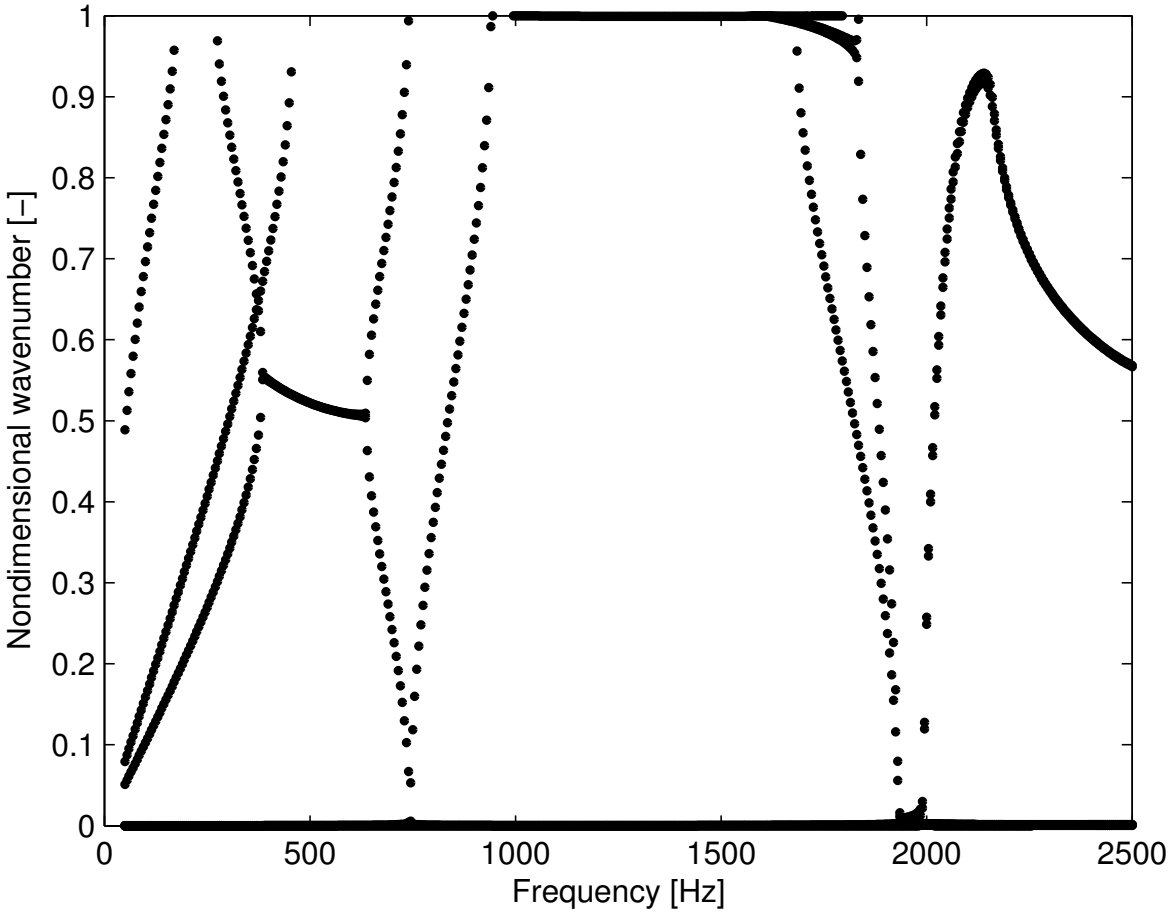

Figure 4. Dispersion analysis of the open circuit system along $\Gamma - X$ ($\varphi = 0$) with no filtering: real part of non dimensional wavenumber vs. frequency [Hz].

the corresponding figures, a color scale is used to show the distribution of modal kinetic energy

$$e_{kin}^{n} = \frac{1}{2}\rho\omega^2 \boldsymbol{u}_n \cdot \boldsymbol{u}_n^* \tag{6}$$

where ρ is the density, $\boldsymbol{u}_n$ is the shape of mode n and $\boldsymbol{u}_n^*$ its conjugate.

In the same frequency range, in-plane shear motion of the cell can also be involved in the movement. This movement is illustrated in figure 7, corresponding to the yellow box highlighted in figure 5.

The last mode that is likely to occur in the same frequency range corresponds to the second flexural mode with anti-symetrical movements of NS and EW legs. It has the lowest wave number of the three described motions and may be interpreted as analogous to the second antisymmetric Lamb-wave mode (A_1) of an homogeneous plate with a very low cut-off frequency (for an elastic plate, the cut-off frequency is defined as the frequency above which higher modes like antisymmetric A_1 or symmetric S_1 appear). The associated shape is shown in figure 8, corresponding to the green box highlighted in figure 5.

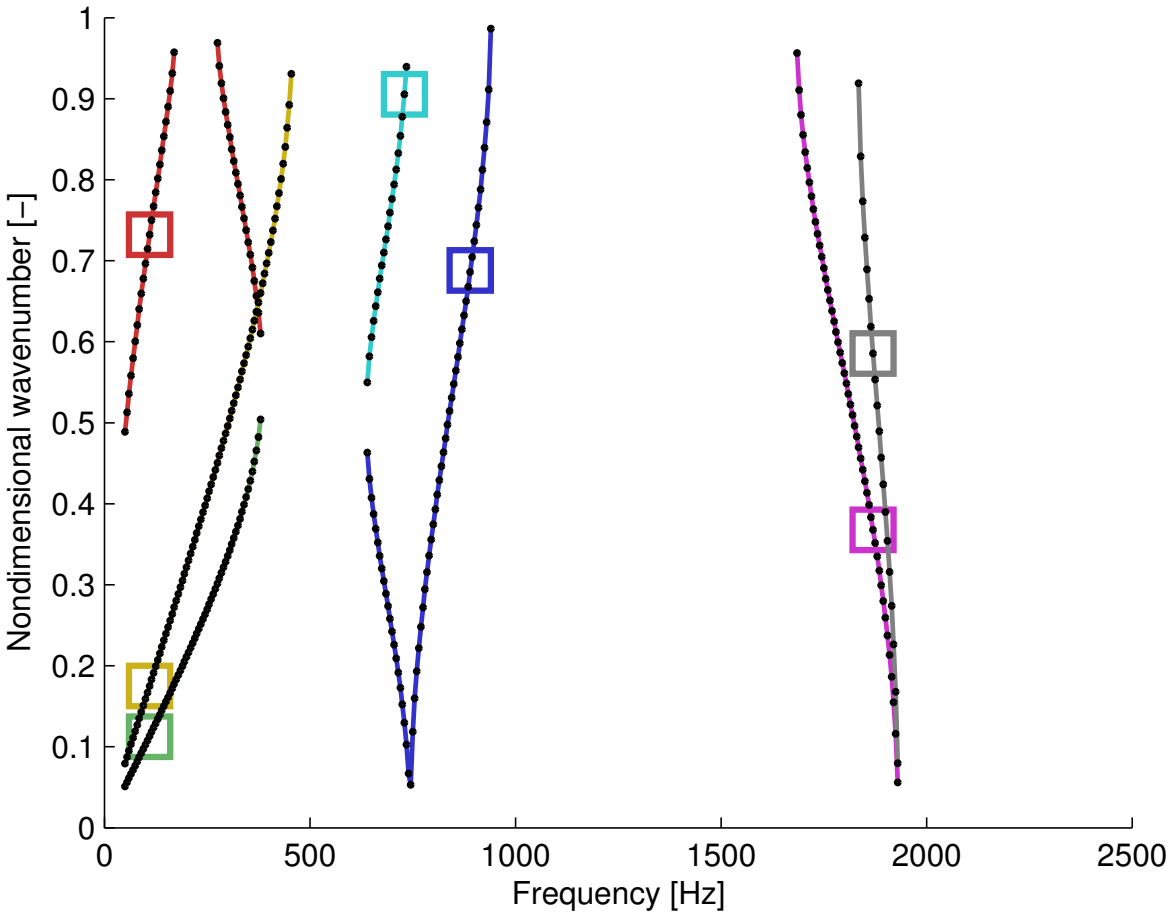

Figure 5. Dispersion analysis of the open circuit system along $\Gamma - X$ ($\varphi = 0$) with filtering: real part of non dimensional wavenumber vs. frequency [Hz]. Square surroundings correspond to solutions whose shapes are shown in figures 6 to 12.

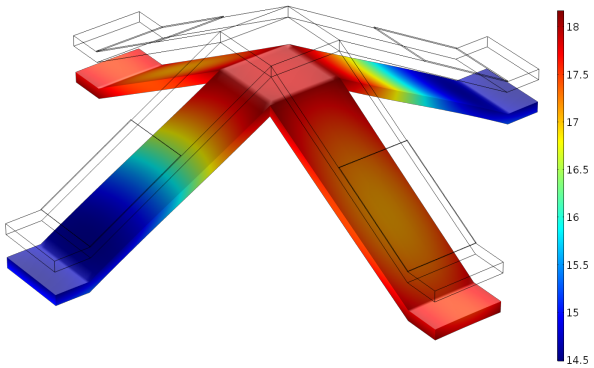

Figure 6. Shape of mode occurring at 110 Hz, with $\text{Real}(k_n) \approx 0.7723\frac{\pi}{L}$, corresponding to red square in figure 5. Color scale corresponds to modal kinetic energy density. Grey lines show the undeformed cell.

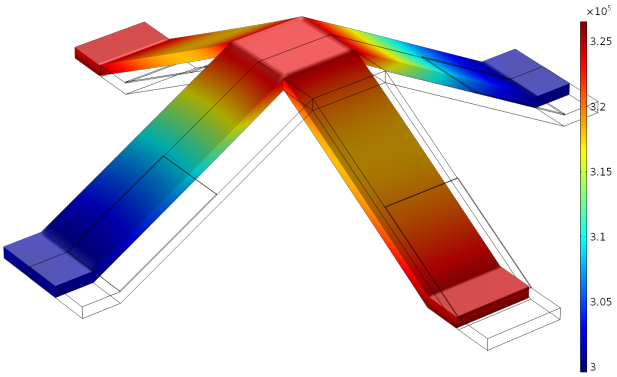

Figure 7. Shape of mode occurring at 110 Hz, with Real(k_n) $\approx 0.1751\frac{\pi}{L}$, corresponding to yellow square in figure 5. Color scale corresponds to modal kinetic energy density. Grey lines show the undeformed cell.

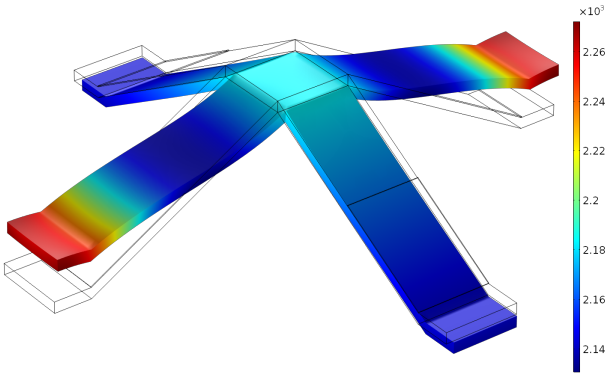

Figure 8. Shape of mode occurring at 110 Hz, with Real(k_n) $\approx 0.1751\frac{\pi}{L}$, corresponding to green square in figure 5. Color scale corresponds to modal kinetic energy density. Grey lines show the undeformed cell.

These three modes may participate to the response of the lattice up to 460 Hz. Between 460 and 650 Hz, a first band gap occurs, with a width to mean frequency ratio equals to 34%. Then, two branches appear, one corresponding to the second flexural mode (see figure 9, associated to cyan square in diagram 5) and to the first torsional mode which is shown in figure 10, corresponding to blue square highlighted in figure 5.

A second band gap then occurs between 950 and 1680 Hz, corresponding to a width to mean ratio equals to more than 55%, which is very high and may be efficiently used for practical filtering applications.

Still going up in frequency range brings the second torsional mode, illustrated in figure 11 and corresponding to purple square in figure 5. It may be emphasized that this mode generates electric charges only in the W and E piezoelectric patches, the N and S ones being almost unstrained. This point will explain some of the observations described in section 5.

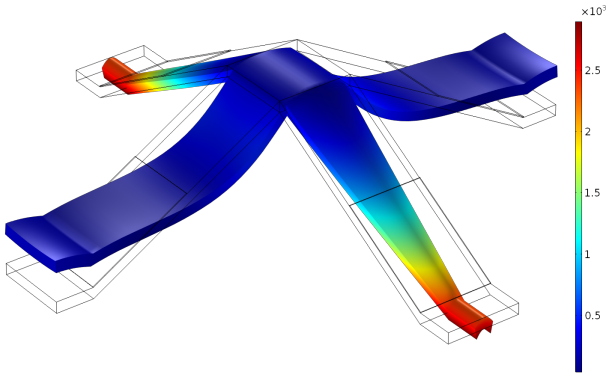

Figure 9. Shape of mode occurring at 730 Hz, with Real(k_n) $\approx 0.9053\frac{\pi}{L}$, corresponding to cyan square in figure 5. Color scale corresponds to modal kinetic energy density. Grey lines show the undeformed cell.

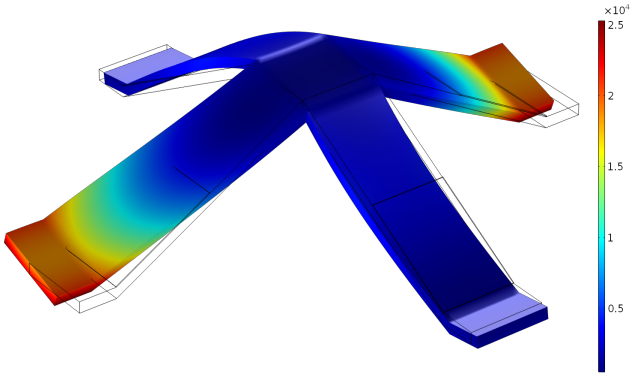

Figure 10. Shape of mode occurring at 890 Hz, with Real(k_n) $\approx 0.686\frac{\pi}{L}$, corresponding to blue square in figure 5. Color scale corresponds to modal kinetic energy density. Grey lines show the undeformed cell.

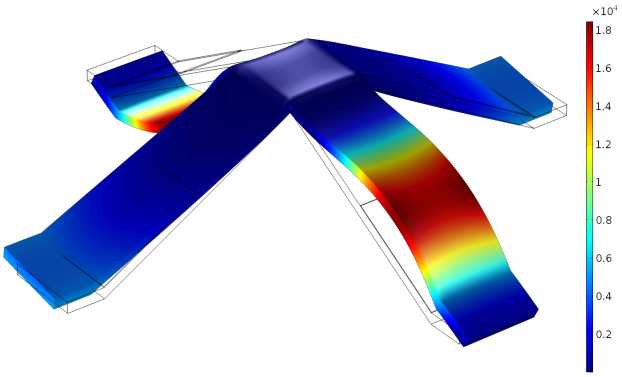

Figure 11. Shape of mode occurring at 1870 Hz, with Real(k_n) $\approx 0.3678\frac{\pi}{L}$, corresponding to purple square in figure 5. Color scale corresponds to modal kinetic energy density. Grey lines show the undeformed cell.

Close to the previous torsion dispersion line, the third flexural mode is observed, as seen in figure 12, corresponding to the gray box highlighted in figure 5. It involves strain mainly in N and S piezoelectric patches.

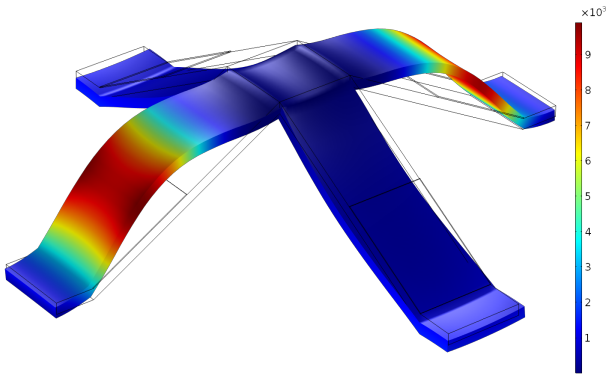

Figure 12. Shape of mode occurring at 1870 Hz, with $\text{Real}(k_n) \approx 0.585678\frac{\pi}{L}$, corresponding to grey square in figure 5. Color scale corresponds to modal kinetic energy density. Grey lines show the undeformed cell.

The last band gap occurring in the frequency range of interest starts around 1950 Hz up to the upper analysis frequency of 2500 Hz.

While the piezoelectric patch is short-circuited, its impact on the dynamical behavior corresponds essentially to an added stiffness at the lower part of the legs. Before discussing the effect of the shunt circuit (see section 5), the behavior of the system in terms of directivity is addressed. A feature that is common to all the wave modes shown above is the fact that the modal deformations are mostly confined to bending and torsion of the ligaments, with global transverse flexural and shear modes. These wave modeshapes are compatible with the mechanical behaviour of the lattice, with the transverse stiffness (Young and shear modulus) significantly lower than the in-plane uniaxial and shear stiffness [54].

4.2. Directivity of the short-circuited reference configuration

By considering only the propagation along $\Gamma - X$ ($\varphi = 0$), the directivity properties of the system can not be observed. A synthetic approach allowing the understanding of the directivity properties of the smart lattice consists in using the evanescence criteria which is computed for each configuration (ω, φ) as

$$Ind(\omega, \varphi) = \min\left\{1, \min_n \frac{|\text{Imag}(k_n)|}{|\text{Real}(k_n)|}\right\}, \tag{7}$$

where n varies over all the computed waves. The saturation with unit value is used since all wave numbers with higher imaginary part than real part are spatially attenuated very rapidly. It should be emphasized that in this directivity analysis, no wave filtering is applied: all possible waves (among which out-of-plane, in-plane, shear movements) are

provided by the calculation and included in the analysis. As a consequence, when the indicator Ind is close to 1, no wave can propagate in the system, whatever the excitation is: only highly evanescent waves can be involved in the movement of the structure.

Figure 13 shows the directivity diagram. In the frequency range of interest, the system exhibits a behavior with a reduced signature in terms of directivity: before 460 Hz, waves can propagate along any direction in the plane. The non-omnidirectional character of the lattice can be observed starting from the second band gap observed in figure 5: between 950 Hz and 1250 Hz, no wave can propagate along the $\varphi = 0$ direction, while the analysis performed for $\varphi = 45°$ shows that the waves are not filtered in this direction below 1250 Hz. Hence the system acts as a mechanical filter in this band. Above 1250 Hz (and below 2500 Hz which is the maximum frequency used in the analysis), the lattice is almost omnidirectional with the band gaps already commented for $\varphi = 0$.

5. Analysis of the shunted device: pure Cneg case

In this section, a pure negative capacitance (Cneg) shunt is used and the dispersion analysis is performed for two cases:

- case EW: only E and W patches are shunted (ie patches aligned with the $\varphi = 0$ direction, the NS patches are still short-circuited;
- case EWNS : all patches are shunted.

5.1. Dispersion along $\Gamma - X$ direction of the lattice embedding a pure Cneg shunt

The figure 14 provides the dispersion diagrams of the three configurations (all patches short-circuited, EW shunts and EWNS shunts).

As expected, the Cneg shunt has a strong impact on the dynamics of the lattice. In the low frequency range, the in-plane shear mode presented in figure 7 is not changed by the shunt since the piezoelectric patches are not strained (see yellow curve in the reference diagram of figure 5). A similar effect may be observed on the first torsional mode whose wavelength is long enough to generate almost no charge between the electrodes (see initial blue curve in figure 5 and associated mode shape in figure 10). All other branches are strongly affected by the shunt, whose main effect is to couple the various modes involving strain in the lowest part of the legs of the kirigami structure. The figure 15 illustrates this by showing the shape of the modified branch at 170 Hz, involving coupling between the out-of-plane shear mode (see figure 6) and the first bending mode shown in figure 8).

In the low frequency region, using only EW shunts provides almost the same effects as if the full EWNS shunts would have been used (this comment is only valid for waves propagating along $\Gamma - X$ direction, see next section for other directions). The difference between EW and EWNS shunts effects can be observed on the second torsional mode and third flexural mode. The second torsional mode, as seen in purple curve in figure

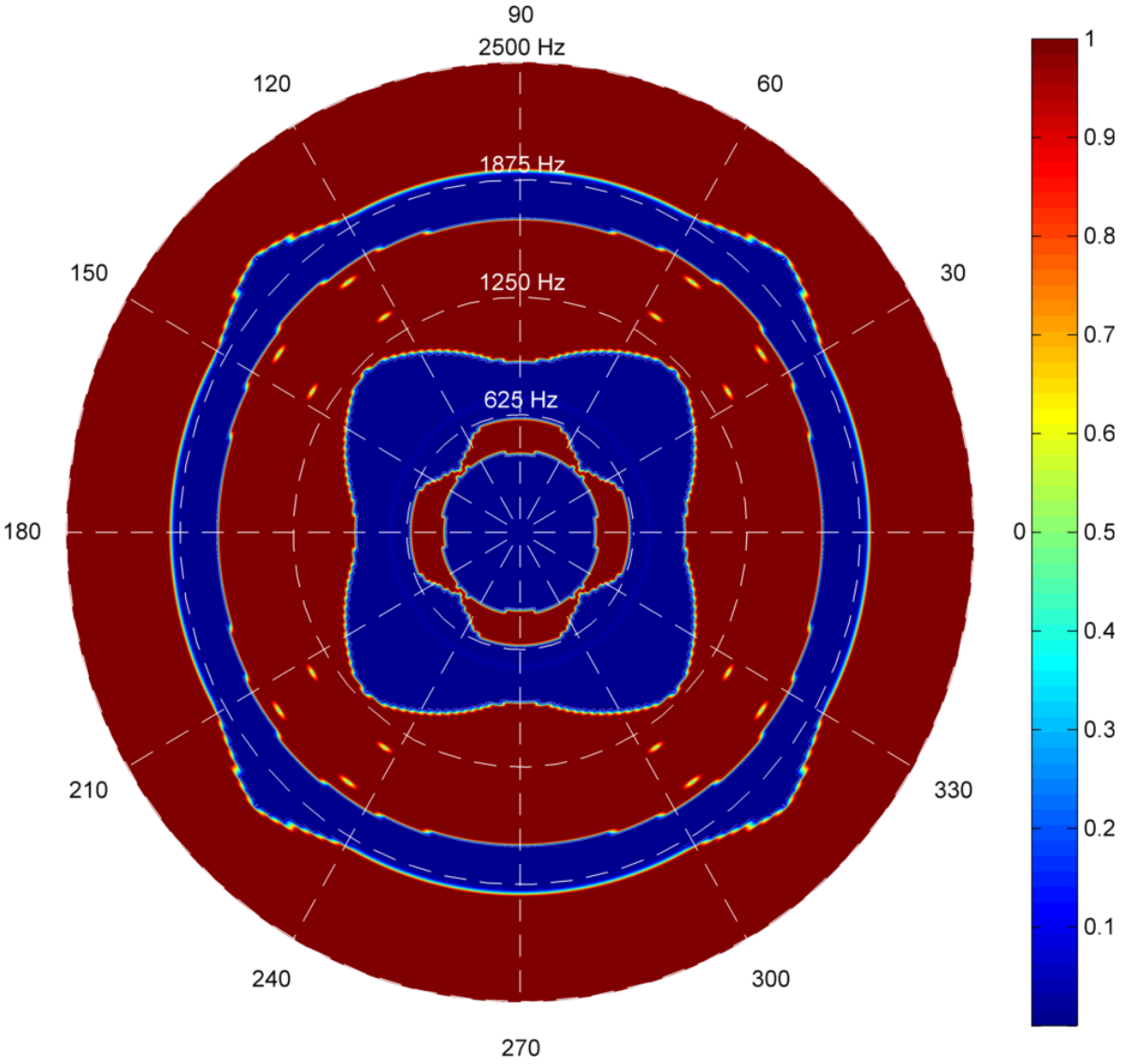

Figure 13. Directivity diagram of the short-circuited system. Distance from the center is frequency. Color is *Ind* (blue: some waves can propagate in the lattice, red: band gap).

5 and associated shape in figure 11), can be controlled only by NS shunts, since EW shunts are not strained while NS ones are located in the area where the strain energy is very high. This implies that the dispersion properties of this mode are impacted only if NS patches are shunted. On the opposite, controlling the third flexural mode (see gray box in figure 5 and shape in figure 12) requires EW shunts while NS shunts have almost no effect, as seen in figure 14. The most interesting feature of the shunted EWNS configuration lies in the fact that, despite the cancellation of the first band gap due to strong modes coupling, the second and third ones are combined, resulting in a large frequency band where no wave can propagate from 1100 Hz to more than 2500 Hz. Further analysis has shown that the upper limit of the band gap in $\Gamma - X$ direction was

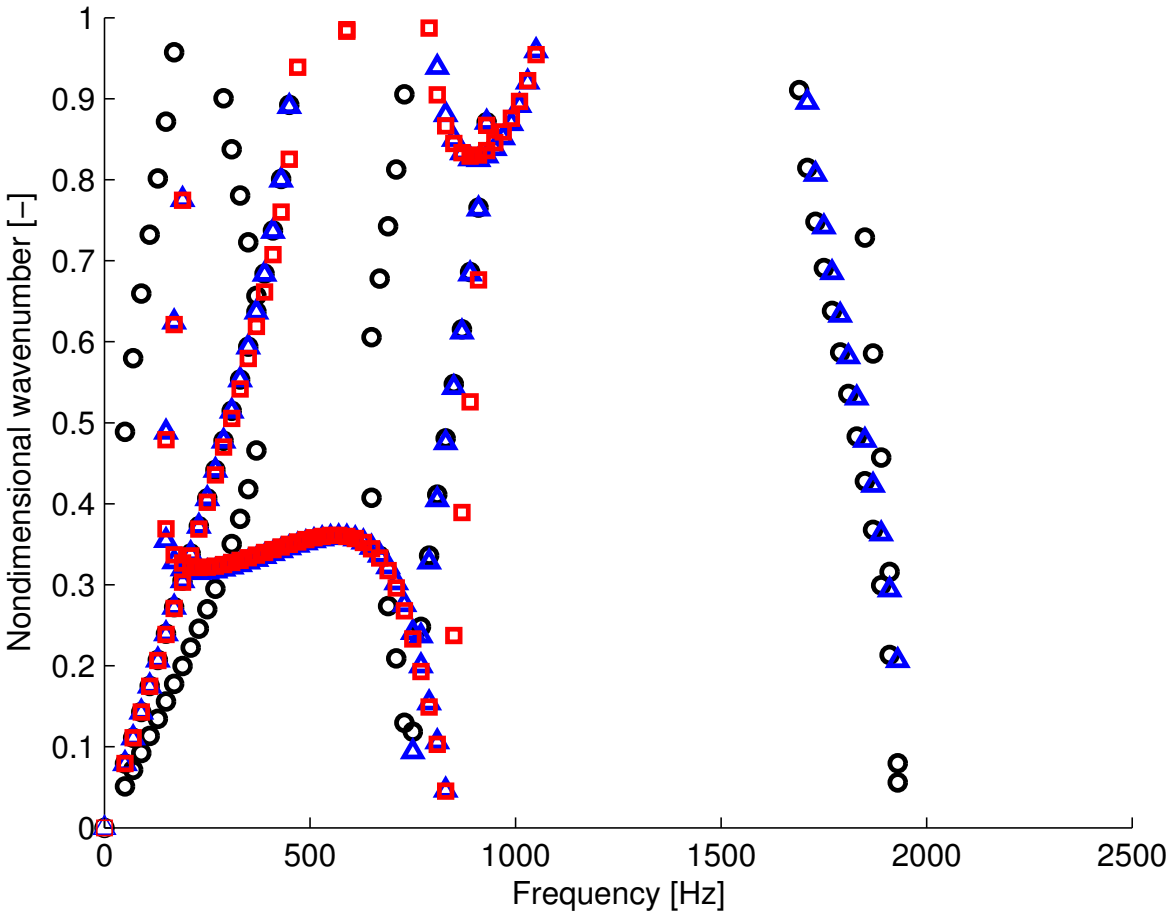

Figure 14. Dispersion analysis along $\Gamma - X$ ($\varphi = 0$) of the shunted system with pure negative capacitance ($R = 0$): real part of non dimensional wavenumber vs. frequency [Hz]. Short circuit (black ○), EW shunts (blue △), EWNS shunts (red □).

2900 Hz, corresponding to an impressive width to mean frequency ratio equals to 90%. The thin pass band below 2kHz for the EW configuration may be used for frequency filtering, providing that practical applications that would take advantage of this, involve deformations of the cell in coherence with the second torsional mode.

5.2. Directivity of the lattice embedding a pure Cneg shunt

The radical changes in the dispersion properties due to the negative capacitance shunt commented in the previous section imply strong evolutions of the directivity diagram, as illustrated in figures 16 for EW shunt and 17 for EWNS shunt. When only the E and W patches are shunted, the low frequency contents below 1000 Hz are highly dependent of φ, meaning that the directional character of the lattice is strong. Above his value, the band gaps are almost omnidirectional. The very selective character of the thin pass band just below 2 kHz is confirmed in a quite omnidirectional way.

This characteristic is more marked for the fully shunted configuration: in this case,

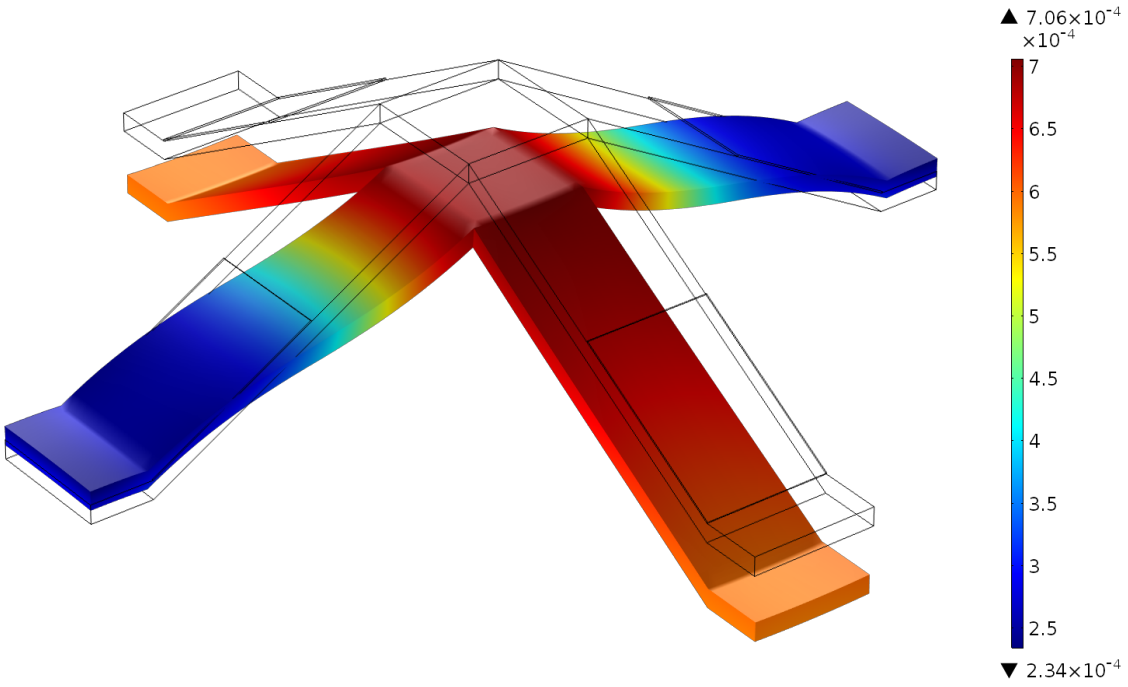

Figure 15. Shape of mode occurring at 170 Hz, with Real(k_n) $\approx 0.3286\frac{\pi}{L}$, for the EW pure Cneg shunt configuration. Color scale corresponds to modal kinetic energy density. Grey lines show the undeformed cell.

starting from 1kHz up to more than 2.5 kHz, no wave can propagate in the system, meaning that a huge omnidirectional band gap has been obtained thanks to the Cneg piezo-shunt embedded on the kirigami lattice. Many practical applications may take advantage of this very large band gap.

6. Impact of resistance in the shunt circuit

The combination of the previous negative capacitance with a resistance in the shunt circuit adds further dissipation to the system. Hence only some little changes may be observed on the real part of the wave numbers, as shown in figure 18 for propagation along $\Gamma - X$. This figure is based on the plot shown in figure 14 on which the new computed wave numbers (including the resistance in the shunt) have been added.

On the other hand, when looking at the imaginary part of the wave numbers it is quite evident to observe that the resistance in the shunt increases the value of the damping by two orders of magnitude for almost all branches of the diagram compared with the pure Cneg case, as shown in figure 19, on which the non dimensional value of the imaginary part is obtained following the same strategy as for the real part. Similar trends as those described in the previous section are observed: depending on the correlation between the strain energy and piezoelectric patches' locations, the shunt has a variable degree of control of the modes. By using the full EWNS shunts one can

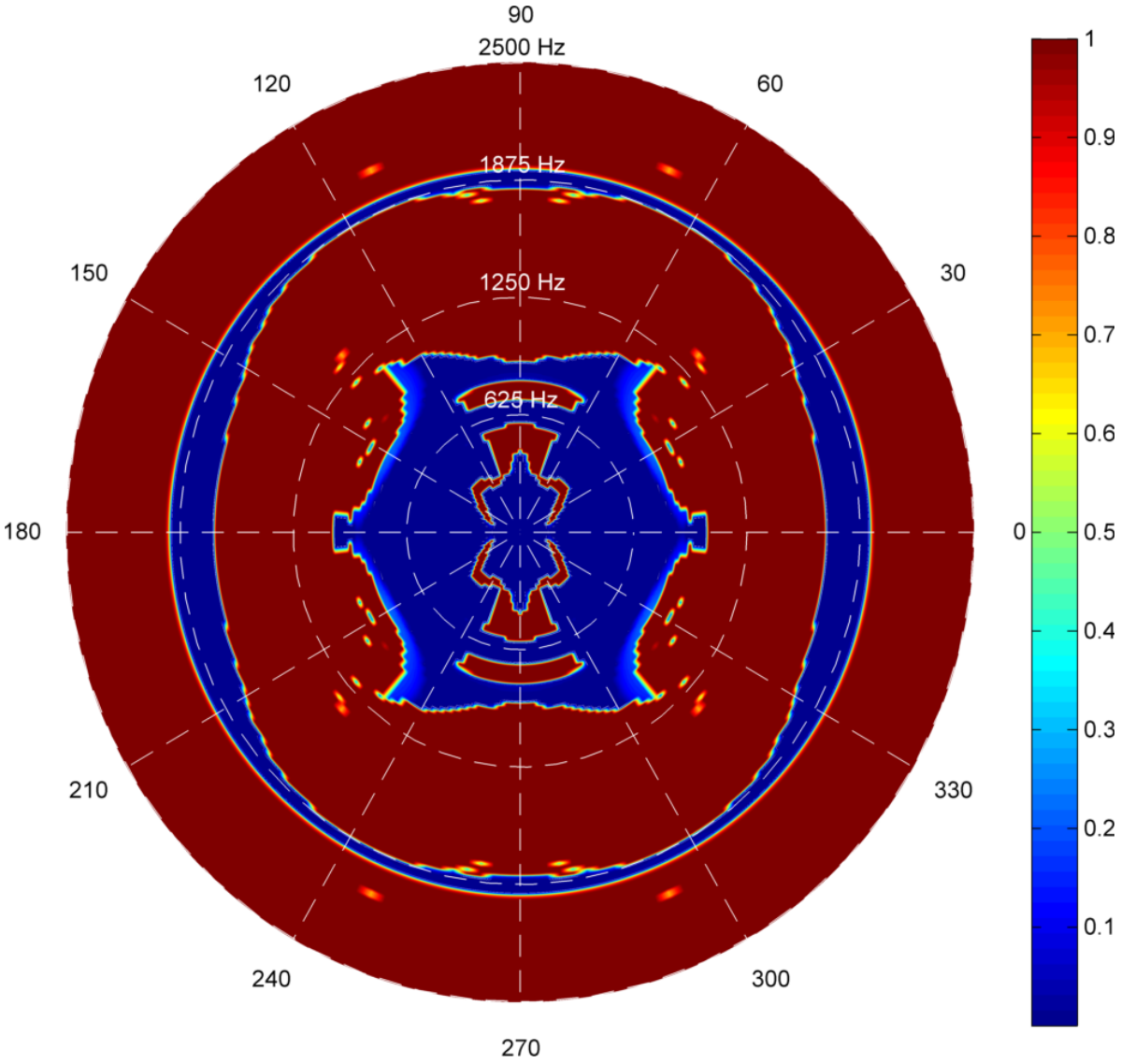

Figure 16. Directivity diagram of the Cneg shunted lattice (only E and W patches are shunted here). Distance from the center is frequency. Color is Ind (blue: some waves can propagate in the lattice, red: band gap).

achieve the ability to control all the waves in the frequency band of interest.

This added damping will clearly act on the directivity of the system, by smoothing the bounds of the gap, as it can be observed in figure 20, which shows the directivity diagram for the RCneg EW shunted lattice. Comparing these results with the ones in figures 13 and 16 it appears that in terms of directivity, the resistance somehow deteriorates the performances of the negative capacitance, by removing the small gaps in the low frequency range, and decreasing the value of the Ind criteria in the second gap, even if for almost all points the decrease remains high with Ind higher than 0.3, still corresponding to a relatively high spacial decay rate of the waves amplitudes.

Adding RCneg shunt on the S and N patches do not change fundamentally the

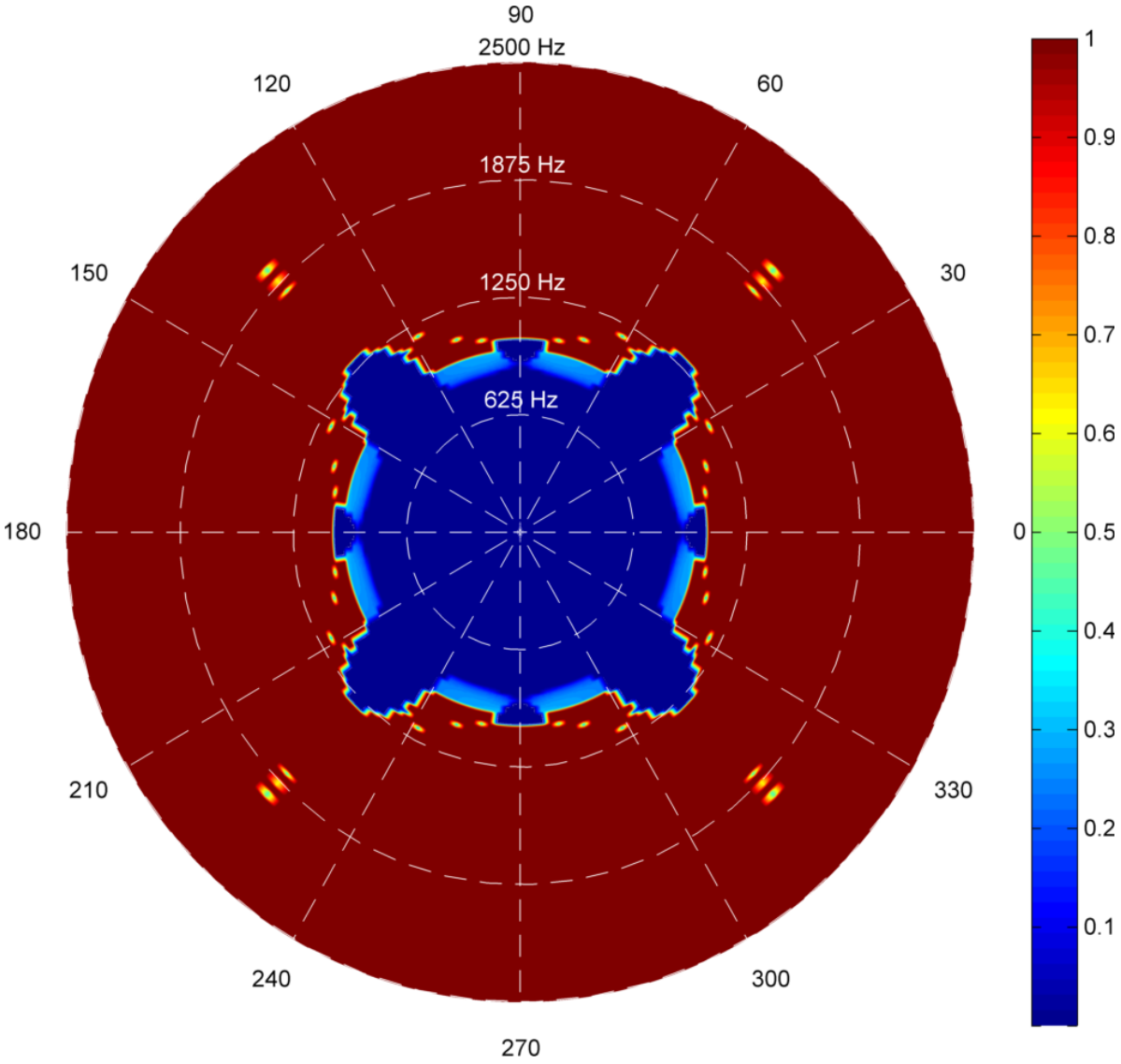

Figure 17. Directivity diagram of the Cneg fully shunted lattice. Distance from the center is frequency. Color is *Ind* (blue: some waves can propagate in the lattice, red: band gap).

behavior of the smart lattice. As shown in figure 21, the trends are similar to the previous case where only E and O patches were shunted. However it seems that a very thin path opened on the whole frequency range (ie. with no band gap) may be obtained for $\varphi = \pi/4$, while waves trying to propagate between 1 kHz and 2.5 kHz along other directions are highly damped, which could be of interest for some practical applications. Further investigations are however required to check the impact of the resistance value on this interesting behavior.

Modifications of waves directivity by added dissipation into the system has already been oberved in [68]. In these two works, dissipation modifies the 2D propagation maps by creating specific frequency dependant directivity or as here opening a $\pi/4$ degree

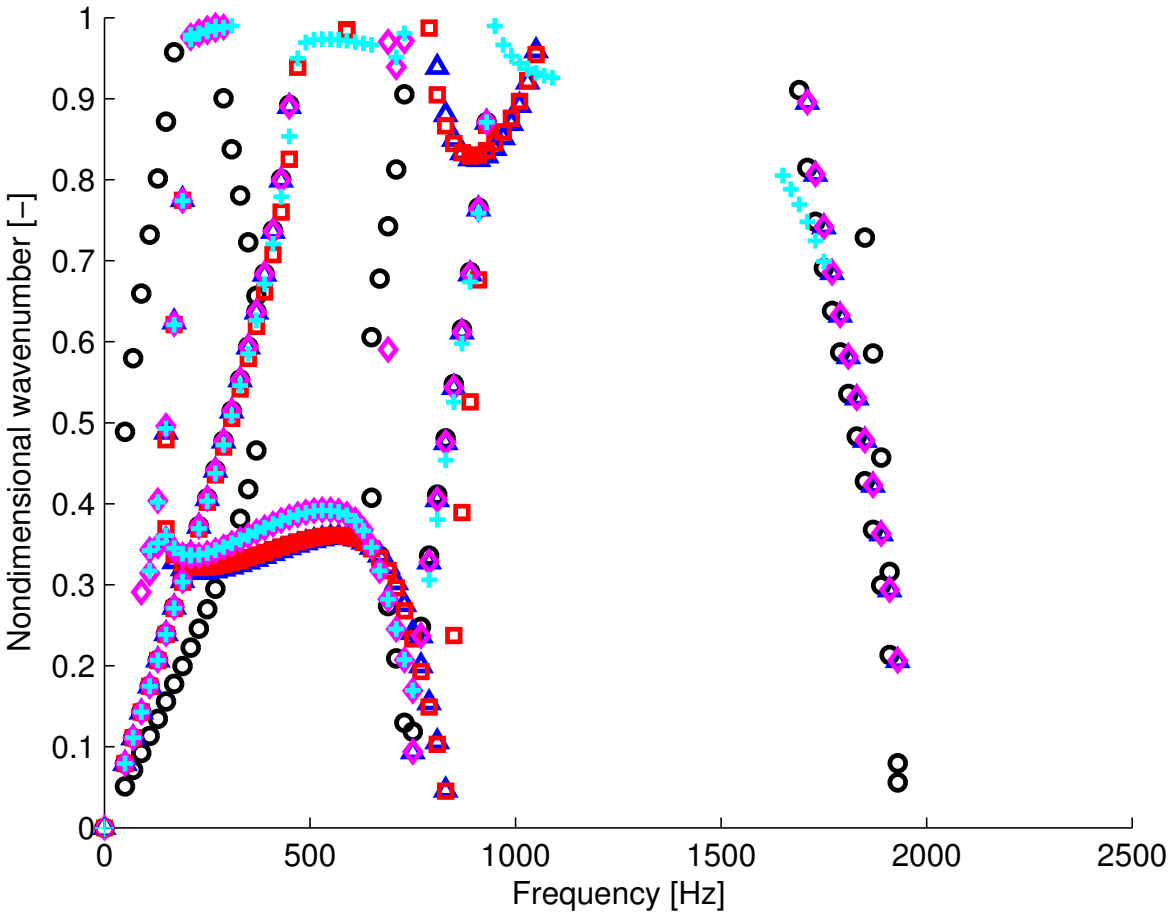

Figure 18. Dispersion analysis along $\Gamma - X$ ($\varphi = 0$) of the shunted system with resistance and negative capacitance ($R = 500\Omega$): real part of non dimensional wavenumber vs. frequency [Hz]. Short circuit (black ○), EW Cneg (blue △), EWNS Cneg shunts (red □), EW RCneg shunts (pink ◊), EWNS RCneg shunts (cyan +).

propagtion door on the whole frequency band of interest especially inside the bands gaps. This phenomenum can be use for filtering vibration even if the damping may induces a strong decay rate of the waves amplitudes.

7. Conclusions

The kirigami pyramidal auxetic active core described in this work has shown promising properties in terms of wave propagation, especially at low frequency badwidths. Various configurations have been investigated, corresponding to either short-circuited, EW or EWNS shunts. Shifting from one configuration to another in a practical implementation is very easy since only electrical shunts are involved. The behaviors observed are higly dependent of the configurations, opening the path to systems embedding devices with efficient adaptive filtering properties. Starting from a deep analysis of the short-circuited configuration, the effect of the shunts has been found to be coherent with the physical

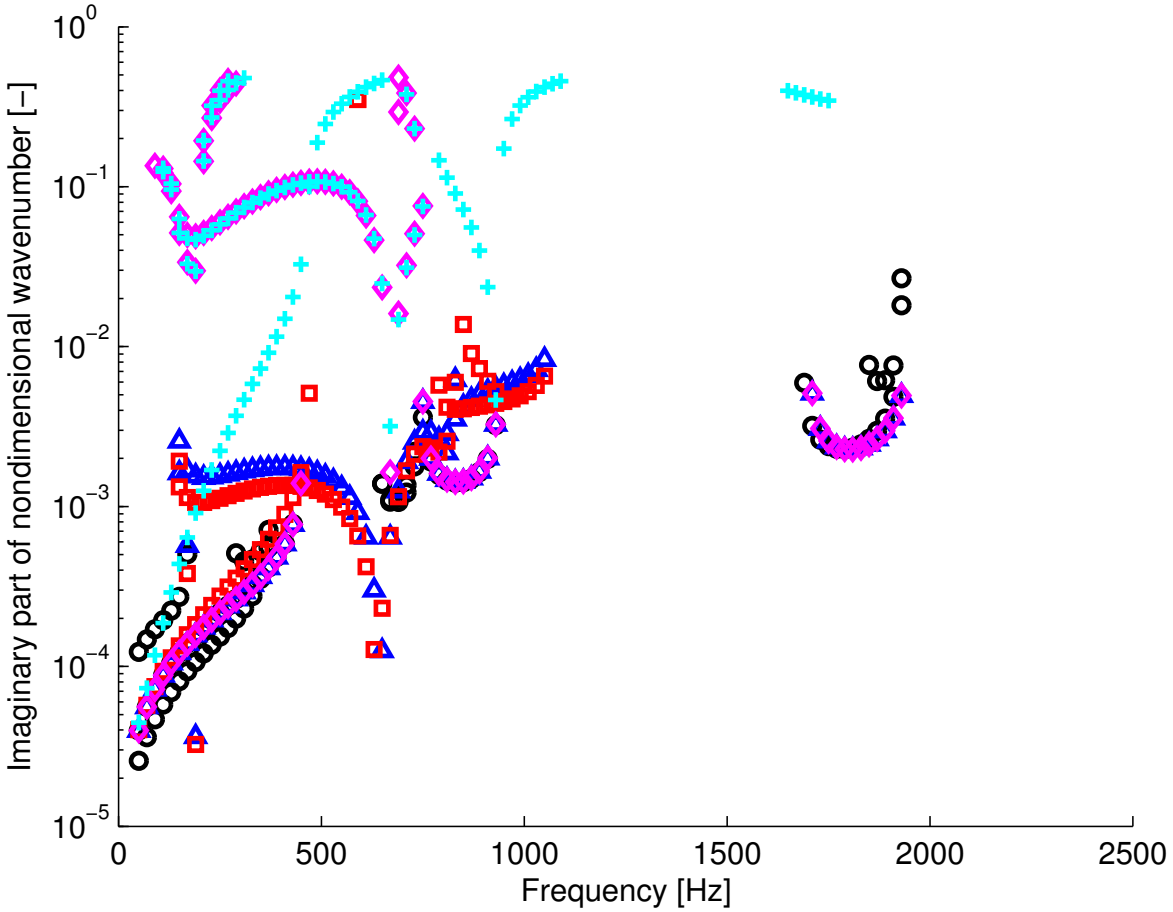

Figure 19. Dispersion analysis along $\Gamma - X$ ($\varphi = 0$) of the shunted system with resistance and negative capacitance ($R = 500\,\Omega$): imaginary part of non dimensional wavenumber vs. frequency [Hz]. Short circuit (black ○), EW shunts (blue +), EWNS shunts (red □).

principles which are involved.

The short-circuited configuration exhibits a behavior with a small directivity signature. The non-omnidirectional character of the lattice can be observed starting from the second band gap, and it has been observed that the waves are not filtered if propagating at $\varphi = 45°$ below 1250 Hz. Several band gaps are observed in this configuration, but remain small in width compared with those that may be obtained with the shunts.

The negative capacitance shunt provides very interesting features since, despite the cancellation of the first band gap due to strong modes coupling, the upper band gaps are combined, resulting in a huge frequency band where no wave can propagate from 1100 Hz to 2900 Hz. Also, a very selective thin pass band below 2kHz for the EW configuration has been observed.

Adding a resistance in the shunt circuit somehow deteriorates the performances of the negative capacitance by removing the small gaps in the low frequency range.

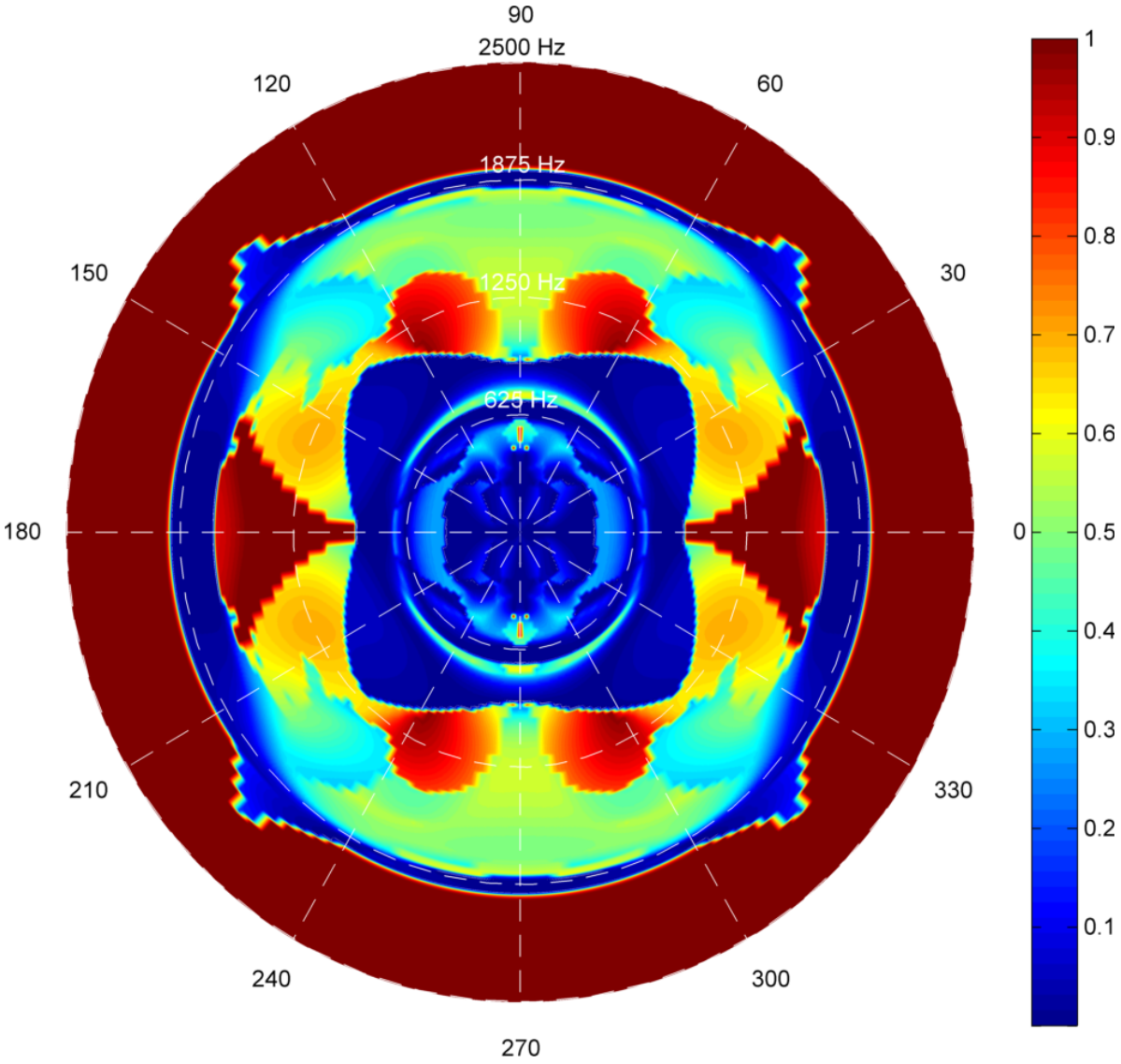

Figure 20. Directivity diagram of the RCneg EW shunted lattice. Distance from the center is frequency. Color is *Ind* (blue: some waves can propagate in the lattice, red: band gap).

It provides however a quite interesting feature, namely the path at $\varphi = 45°$ which is extended to the whole frequency band of interest.

Acknowledgments

A part of this work was financed by The French National Research Agency under grant number ANR-12-JS09-008-COVIA. It has been performed in cooperation with the Labex ACTION program (ANR-11-LABX-0001-01). Fabrizio Scarpa thanks the support of the FP7-NMP3-LA-2010-246067 project for the logistics of the kirigami lattice design. The Authors would also like to thank the anonymous reviewers for the helpful suggestions.

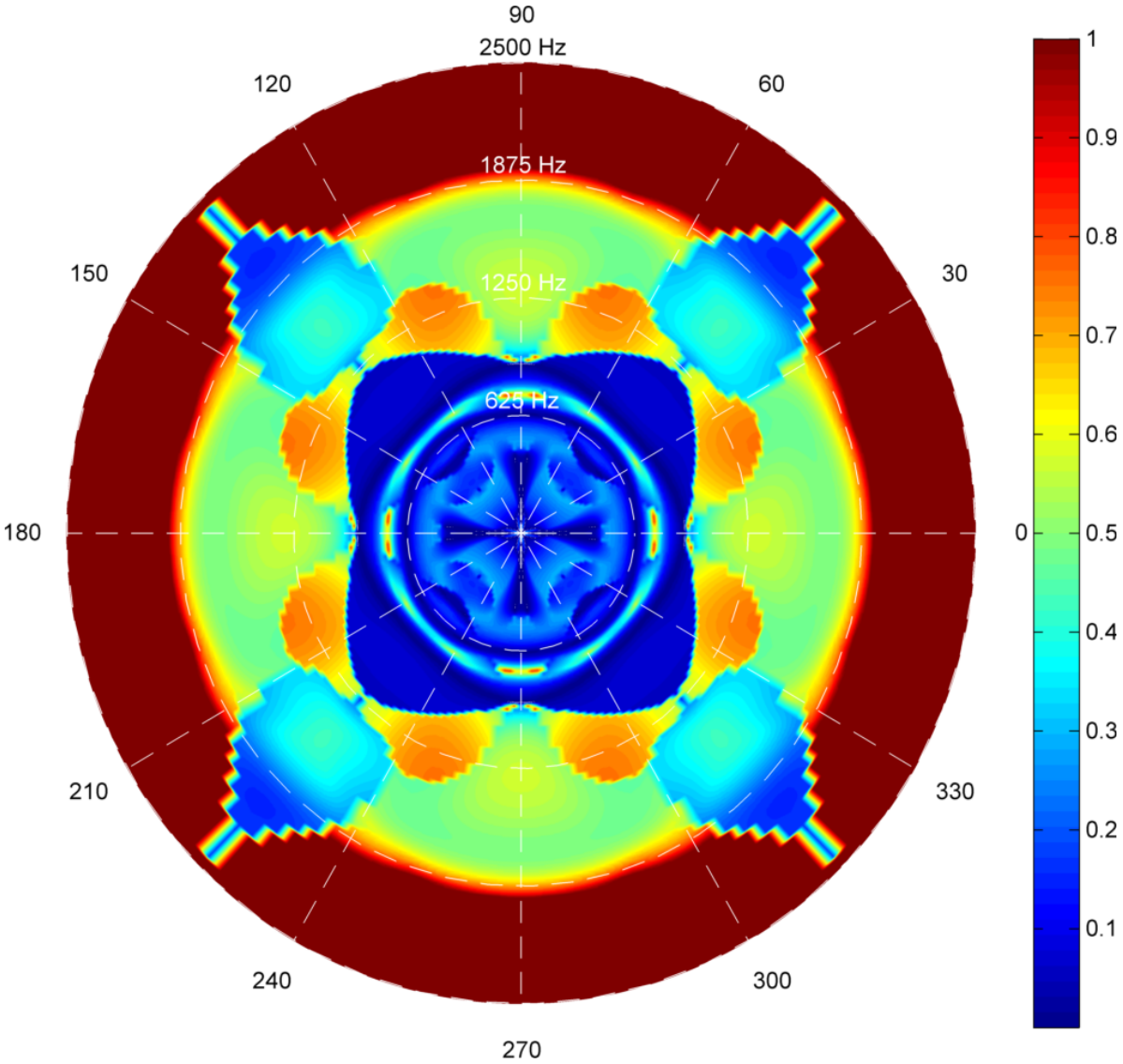

Figure 21. Directivity diagram of the RCneg fully shunted lattice. Distance from the center is frequency. Color is *Ind* (blue: some waves can propagate in the lattice, red: band gap).

References

[1] A. Preumont. *Vibration control of structures : An introduction*. Kluwer, 1997.

[2] P.A. Nelson and S.J. Elliott. *Active Control of Sound*. Pub. Academic Press, London, San Diego, 1992.

[3] H.T. Banks, R.C. Smith, and Y. Wang. *Smart material structures Modeling Estimation and Control*. Masson and Wiley, 1996.

[4] O. Thorp, M. Ruzzene, and A. Baz. Attenuation and localization of wave propagation in rods with periodic shunted piezoelectric patches. *Smart Materials and Structures*, 10(5):979, 2001.

[5] M. Collet, K.A. Cunefare, and N.M. Ichchou. Wave Motion Optimization in Periodically Distributed Shunted Piezocomposite Beam Structures. *Journal of Int Mat Syst and Struct*, 20(7):787–808, 2009.

[6] S. Yang, J.H. Page, Z. Liu, M.L. Cowan, C.T. Chan, and P. Sheng. Ultrasound tunneling through 3D phononic crystals. *Physical Review Letters*, 88(10):104301, 2002.

[7] Z. Liu, X. Zhang, Y. Mao, Y.Y. Zhu, Z. Yang, C.T. Chan, and P. Sheng. Locally resonant sonic materials. *Science*, 289(5485):1734–1736, 2000.

[8] N. Fang, D. Xi, J. Xu, M. Ambati, W. Srituravanich, C. Sun, and X. Zhang. Ultrasonic metamaterials with negative modulus. *Nature Materials*, 5(6):452–456, 2006.

[9] M. Ambati, N. Fang, C. Sun, and X. Zhang. Surface resonant states and superlensing in acoustic metamaterials. *Physical Review B*, 75(19):195447, 2007.

[10] X. Hu, C.T. Chan, and J. Zi. Two-dimensional sonic crystals with helmholtz resonators. *Physical Review E*, 71(5):556, 2005.

[11] M.I. Hussein, M.J. Leamy, and M. Ruzzene. Dynamics of phononic materials and structures: Historical origins, recent progress, and future outlook. *Applied Mechanics Reviews*, 66(4):040802, 2014.

[12] C.H. Park and A. Baz. Vibration control of beams with negative capacitive shunting of interdigital electrode piezoceramics. *Journal of Vibration and Control*, 11(3):331–346, 2005.

[13] N.W. Hagood and A. von Flotow. Damping of structural vibrations with piezoelectric materials and passive electrical networks. *Journal of Sound and Vibration*, 146(2):243–268, 1991.

[14] F. Casadei, M. Ruzzene, L. Dozio, and K.A. Cunefare. Broadband vibration control through periodic arrays of resonant shunts: experimental investigation on plates. *Smart Materials and Structures*, 19(1):150, 2010.

[15] A. Spadoni, M. Ruzzene, and K.A. Cunefare. Vibration and wave propagation control of plates with periodic arrays of shunted piezoelectric patches. *Journal of Intelligent Material Systems and Structures*, 20(8):979–990, 2009.

[16] S. Chen, G. Wang, J. Wen, and X. Wen. Wave propagation and attenuation in plates with periodic arrays of shunted piezo-patches. *Journal of Sound and Vibration*, 332(6):1520–1532, 2013.

[17] G. Wang and S. Chen. Large low-frequency vibration attenuation induced by arrays of piezoelectric patches shunted with amplifier–resonator feedback circuits. *Smart Materials and Structures*, 25(1):015004, 2015.

[18] R. Zhu, Y.Y. Chen, M.V. Barnhart, G.K. Hu, C.T. Sun, and G.L. Huang. Experimental study of an adaptive elastic metamaterial controlled by electric circuits. *Applied Physics Letters*, 108(1):011905, 2016.

[19] R.L. Forward. Electronic damping of vibrations in optical structures. *Applied Optics*, 18(5):690–697, 1979.

[20] S. Livet, M. Collet, M. Berthillier, P. Jean, and J.M. Cote. Structural multi-modal damping by optimizing shunted piezoelectric transducers. *European Journal of Computational Mechanics*, 20(1-4):73–102, 2011.

[21] M. Collet, M. Ouisse, and M.N. Ichchou. Structural energy flow optimization through adaptive shunted piezoelectric metacomposites. *Journal of Intelligent Material Systems and Structures*, 23(15):1661–1677, 2012.

[22] E. Fukada, M. Date, K. Kimura, T. Okubo, H. Kodama, P. Mokry, and K. Yamamoto. Sound isolation by piezoelectric polymer films connected to negative capacitance circuits. *IEEE Transactions on Dielectrics and Electrical Insulation*, 11(2):328–333, 2004.

[23] J. Kim and Y.C. Jung. Broadband noise reduction of piezoelectric smart panel featuring negative-capacitive-converter shunt circuit. *The Journal of the Acoustical Society of America*, 120(4):2017–2025, 2006.

[24] B. S. Beck, K. A. Cunefare, and M. Collet. Response-based tuning of a negative capacitance shunt for vibration control. *Journal of Intelligent Material Systems and Structures*, 25:1585–1595, 2014.

[25] F. Tateo, M. Collet, M. Ouisse, M.N. Ichchou, K. Cunefare, and P. Abbe. Experimental characterization of a bi-dimensional array of negative capacitance piezo-patches for vibroacoustic control. *Journal of Intelligent Material Systems and Structures*, 21, 2014.

[26] F. Tateo, M. Collet, M. Ouisse, and K.A. Cunefare. Design variables for optimizing adaptive metacomposite made of shunted piezoelectric patches distribution. *Journal of Vibration and Control*, 2014.

[27] M. Collet, M. Ouisse, and F. Tateo. Adaptive metacomposites for vibroacoustic control applications. *IEEE Sensors Journal*, 14(7):2145–2152, 2014.

[28] M. Collet, M. Ouisse, M.N. Ichchou, and R. Ohayon. Semi-active optimization of 2D wave dispersion into shunted piezo-composite systems for controlling acoustic interaction. *Smart Materials and Structures*, 21(9):94, 2012.

[29] H. Zhang, J. Wen, Y. Xiao, G. Wang, and X. Wen. Sound transmission loss of metamaterial thin plates with periodic subwavelength arrays of shunted piezoelectric patches. *Journal of Sound and Vibration*, 343:104–120, 2015.

[30] B. Lossouarn, J.F. Deü, and M. Aucejo. Multimodal vibration damping of a beam with a periodic array of piezoelectric patches connected to a passive electrical network. *Smart Materials and Structures*, 24(11):115037, 2015.

[31] B. Lossouarn, M. Aucejo, and J.F. Deü. Multimodal coupling of periodic lattices and application to rod vibration damping with a piezoelectric network. *Smart Materials and Structures*, 24(4):045018, 2015.

[32] T. Toffoli and N. Margolus. Programmable matter: Concepts and realization. *Physica D: Nonlinear Phenomena*, 47(1-2):263–272, 1991.

[33] K. Miura. Method of packaging and deployment of large membranes in space. *title The Institute of Space and Astronautical Science report*, 618:1, 1985.

[34] K. Miura and Y. Miyazaki. Concept of the tension truss antenna. *AIAA journal*, 28(6):1098–1104, 1990.

[35] T. Nojima and K. Saito. Development of newly designed ultra-light core structures. *JSME International Journal Series A Solid Mechanics and Material Engineering*, 49(1):38–42, 2006.

[36] K. Saito, F. Agnese, and F. Scarpa. A cellular kirigami morphing wingbox concept. *Journal of Intelligent Material Systems and Structures*, 22(9):935–944, 2011.

[37] Y. Hou, R. Neville, F. Scarpa, C. Remillat, B. Gu, and M. Ruzzene. Graded conventional-auxetic kirigami sandwich structures: Flatwise compression and edgewise loading. *Composites Part B: Engineering*, 59:33 – 42, 2014.

[38] C. Jianguo, D. Xiaowei, and F. Jian. Morphology analysis of a foldable kirigami structure based on miura origami. *Smart Materials and Structures*, 23(9):094011, 2014.

[39] S. Sareh and J. Rossiter. Kirigami artificial muscles with complex biologically inspired morphologies. *Smart Materials and Structures*, 22(1):014004, 2013.

[40] P.Z. Hanakata, Z. Qi, D.K. Campbell, and H.S. Park. Highly stretchable mos2 kirigami. *Nanoscale*, 8:458–463, 2016.

[41] N. Turner, B. Goodwine, and M. Sen. A review of origami applications in mechanical engineering. *Proceedings of the Institution of Mechanical Engineers, Part C: Journal of Mechanical Engineering Science*, 2015.

[42] R. Lakes. Foam structures with a negative poisson's ratio. *Science*, 235(4792):1038–1040, 1987.

[43] K.E. Evans, M.A. Nkansah, I.J. Hutchinson, and S.C. Rogers. Molecular network design. *Nature*, 353(6340):124–124, 09 1991.

[44] L.J. Gibson and M.F Ashby. The mechanics of three-dimensional cellular materials. In *Proceedings of the Royal Society of London A: Mathematical, Physical and Engineering Sciences*, volume 382, pages 43–59. The Royal Society, 1982.

[45] F. Scarpa, P. Panayiotou, and G. Tomlinson. Numerical and experimental uniaxial loading on in-plane auxetic honeycombs. *The Journal of Strain Analysis for Engineering Design*, 35(5):383–388, 2000.

[46] J.N. Grima, E. Manicaro, and D. Attard. Auxetic behaviour from connected different-sized squares and rectangles. In *Proceedings of the Royal Society of London A: Mathematical, Physical and Engineering Sciences*, volume 467, pages 439–458. The Royal Society, 2011.

[47] U.D. Larsen, O. Signund, and S. Bouwsta. Design and fabrication of compliant micromechanisms and structures with negative poisson's ratio. *Journal of Microelectromechanical Systems*, 6(2):99–106, 1997.

[48] J.N. Grima, R. Gatt, A. Alderson, and K.E. Evans. On the potential of connected stars as auxetic systems. *Molecular Simulation*, 31(13):925–935, 2005.

[49] C. Lira, F. Scarpa, and R. Rajasekaran. A gradient cellular core for aeroengine fan blades based on auxetic configurations. *Journal of Intelligent Material Systems and Structures*, 22(9):907–917, 2011.

[50] D. Prall and R.S. Lakes. Properties of a chiral honeycomb with a poisson's ratio of -1. *International Journal of Mechanical Sciences*, 39(3):305–314, 1997.

[51] Ole Sigmund. Tailoring materials with prescribed elastic properties. *Mechanics of Materials*, 20(4):351–368, 1995.

[52] Luigi Cabras and Michele Brun. Auxetic two-dimensional lattices with poisson's ratio arbitrarily close to- 1. In *Proceedings of the Royal Society of London A: Mathematical, Physical and Engineering Sciences*, volume 470, page 20140538. The Royal Society, 2014.

[53] Luigi Cabras and Michele Brun. A class of auxetic three-dimensional lattices. *Journal of the Mechanics and Physics of Solids*, 91:56–72, 2016.

[54] F. Scarpa, M. Ouisse, M. Collet, and K. Saito. Kirigami auxetic pyramidal core: mechanical properties and wave propagation analysis in damped lattice. *Journal of Vibration and Acoustics*, 135(4):041001, 2013.

[55] K. Virk, A. Monti, T. Trehard, M. Marsh, K. Hazra, K. Boba, C.D.L. Remillat, F. Scarpa, and I.R. Farrow. Silicomb peek kirigami cellular structures: mechanical response and energy dissipation through zero and negative stiffness. *Smart Materials and Structures*, 22(8):084014, 2013.

[56] T.C. Lim. *Auxetic materials and structures*. Springer, 2014.

[57] J. Wen, S. Chen, G. Wang, D. Yu, and X. Wen. Directionality of wave propagation and attenuation in plates with resonant shunting arrays. *Journal of Intelligent Material Systems and Structures*, page 1045389X14560361, 2014.

[58] S.M. Pingle, N.A. Fleck, V.S. Deshpande, and H.N.G. Wadley. Collapse mechanism maps for a hollow pyramidal lattice. *Proceedings of the Royal Society of London A: Mathematical, Physical and Engineering Sciences*, 467(2128):985–1011, 2011.

[59] C.I. Hammetter, R.G. Rinaldi, and F.W. Zok. Pyramidal lattice structures for high strength and energy absorption. *Journal of Applied Mechanics*, 80(4):041015–041015, 05 2013.

[60] S. Yin, L. Wu, and S. Nutt. In-plane compression of hollow composite pyramidal lattice sandwich columns. *Journal of Composite Materials*, 48(11):1337–1346, 2014.

[61] S. Yin, L. Wu, and S. Nutt. Stretch–bend-hybrid hierarchical composite pyramidal lattice cores. *Composite Structures*, 98:153 – 159, 2013.

[62] M. Bilski and K.W. Wojciechowski. Tailoring poisson's ratio by introducing auxetic layers. *physica status solidi (b)*, 2016.

[63] AA Pozniak, J Smardzewski, and KW Wojciechowski. Computer simulations of auxetic foams in two dimensions. *Smart Materials and Structures*, 22(8):084009, 2013.

[64] K.W. Wojciechowski. Constant thermodynamic tension monte carlo studies of elastic properties of a two-dimensional system of hard cyclic hexamers. *Molecular Physics*, 61(5):1247–1258, 1987.

[65] KW Wojciechowski. Two-dimensional isotropic system with a negative poisson ratio. *Physics Letters A*, 137(1-2):60–64, 1989.

[66] K.W. Wojciechowski, K.V. Tretiakov, and M. Kowalik. Elastic properties of dense solid phases of hard cyclic pentamers and heptamers in two dimensions. *Physical Review E*, 67(3):036121, 2003.

[67] M. W. Hooker. Properties of pzt-based piezoelectric properties of pzt-based piezoelectric ceramics between -150 and 250 °c. Technical Report NASA/CR-1998-208708, NASA, 1998.

[68] M. Collet, M. Ouisse, M. Ruzzene, and M.N. Ichchou. A floquet-bloch decomposition of the elastodynamical equations: application to bi-dimensional wave's dispersion computation of

damped mechanical system. *International Journal of Solids and Structures*, 48:2837–2848, 2011.
[69] C. Kittel. *Introduction to Solid State Physics*. John Wiley and Sons, New York, 1986.
[70] W. Maysenhölder. *Körperschallenergie*. Hirzel, Stuttgart, 1994.